PHYSICAL REVIEW D **110,** 123025 (2024)

Simulating the Galactic population of axion clouds around stellar-origin black holes: Gravitational wave signals in the 10–100 kHz band

Jacob R. Sprague,[1,*] Shane L. Larson,[1] Zhiyuan Wang,[2] Shelby Klomp,[2] Andrew Laeuger,[3] George Winstone,[2]
Nancy Aggarwal,[4] Andrew A. Geraci,[2] and Vicky Kalogera[1]

(LSD Collaboration)

[1]*Center for Interdisciplinary Exploration and Research in Astrophysics (CIERA), Department of Physics and Astronomy, Northwestern University, Evanston, Illinois 60208, USA*
[2]*Center for Fundamental Physics, Department of Physics and Astronomy, Northwestern University, Evanston, Illinois 60208, USA*
[3]*The Division of Physics, Mathematics and Astronomy, California Institute of Technology, Pasadena, California 91125, USA*
[4]*Department of Physics and Astronomy, University of California, Davis, Davis, California 95616, USA*

(Received 5 September 2024; accepted 29 October 2024; published 18 December 2024)

Ultralight scalar fields can experience runaway "superradiant" amplification near spinning black holes, resulting in a macroscopic "axion cloud," which slowly dissipates via continuous monochromatic gravitational waves. For a particular range of boson masses, $\mathcal{O}(10^{-11}\text{–}10^{-10})$ eV, an axion cloud will radiate in the 10–100 kHz band of the levitated sensor detector (LSD). Using fiducial models of the mass, spin, and age distributions of stellar-origin black holes, we simulate the present-day Milky Way population of these hypothetical objects. As a first step toward assessing the LSD's sensitivity to the resultant ensemble of gravitational wave signals, we compute the corresponding signal-to-noise ratios which build up over a nominal integration time of 10^7 s, assuming the projected sensitivity of the 1 m LSD prototype currently under construction, as well as for future 10 m and 100 m concepts. For a 100 m cryogenic instrument, hundreds of resolvable signals could be expected if the boson mass μ is around 3×10^{-11} eV, and this number diminishes with increasing μ up to $\approx 5.5 \times 10^{-11}$ eV. The much larger population of unresolved sources will produce a confusion foreground which could be detectable by a 10-m instrument if $\mu \in (3\text{–}4.5) \times 10^{-11}$ eV or by a 100-m instrument if $\mu \in (3\text{–}6) \times 10^{-11}$ eV.

DOI: 10.1103/PhysRevD.110.123025

I. INTRODUCTION

The era of gravitational-wave (GW) astronomy is in full swing. During their first three observing runs, the GW interferometers Advanced LIGO and Advanced Virgo detected 90 compact binary coalescences involving neutron stars (NS) and stellar-mass black holes (BH) [1–3]. The most notable events included the first NS-NS merger (GW170817) [4], the first highly asymmetric binary (GW190412) [5], the first merger with an intermediate-mass BH remnant (GW190521) [6], and the first object in the mass gap separating the most massive neutron stars from the lowest-mass BHs (GW190814) [7]. The first half of the fourth observing run has already seen a new lower-mass-gap event (GW230529) [8].

Adding to the excitement, evidence for a stochastic background has been reported in the 15-year dataset from the North American Nanohertz Observatory for Gravitational Waves [9]. The most well-motivated scenario for the origin of this background is the extragalactic population of inspiralling supermassive BH binaries.

Finally, the launch of the Laser Interferometer Space Antenna (LISA) in the mid-2030s will open up the millihertz band for exploration. The Galactic population of compact binaries—and the extragalactic population of supermassive BH binaries and extreme-mass-ratio-inspirals—are all highly anticipated LISA sources [10].

These observatories cover multiple windows in the GW spectrum from the nanohertz up to several hundred Hz. The push to higher frequencies is now underway, with cosmic strings, axion clouds, primordial black hole (PBH) binaries, and early universe stochastic backgrounds as the main science drivers [11].

One such concept, currently in development at Northwestern University, is the Levitated Sensor Detector (LSD). With sensitivity to GWs at tens to hundreds of kHz,

---

[*] Contact author: JacobSprague2021@u.northwestern.edu

the LSD employs optically trapped micron-scale disks as GW sensors. The instrument is a Michelson interferometer with two perpendicular 1 m Fabry-Pérot arm cavities. In each arm, a disk is levitated at an antinode of a standing-wave formed by two counter-propagating beams. The trapped object behaves like a driven damped harmonic oscillator, with the corresponding trap frequency being widely tunable with laser intensity. The periodic changes in arm length induced by a GW manifest as a periodic shift in the position of the antinode. If the trap frequency matches the GW frequency, the levitated sensor is resonantly driven [12–14].

As a resonant detector, the LSD is well suited to search for continuous monochromatic signals. A popular scenario involves the interaction between spinning black holes and "ultralight" bosonic fields—i.e. those with masses several orders of magnitude smaller than an electron volt (eV). Such fields can extract rotational energy from spinning BHs via "superradiant amplification" of certain bound-states [15]. The result is a macroscopic cloud of bosons all living in the same state—commonly known as a "gravitational atom" or "axion cloud" [16]. These oscillating nonaxisymmetric clouds generate continuous monochromatic GWs at a frequency primarily determined by the boson's mass. Tens to hundreds of kHz corresponds to $\mu = \mathcal{O}(10^{-11}\text{–}10^{-10})$ eV.

This scenario can be realized with physics beyond-the-Standard-Model (BSM). For example, a large number of ultralight fields may occur as a result of the compactification of extra dimensions [17]. One of these may be the QCD axion—the pseudoscalar boson proposed to solve the strong-*CP* problem [18–20]. The axion is a Goldstone boson of a spontaneously broken global symmetry which acquires a small mass through nonperturbative effects. Its mass, μ, is determined by the energy scale f_a associated with the broken symmetry [17],

$$\mu \approx 6\times 10^{-10}\ \text{eV}\left(\frac{10^{16}\ \text{GeV}}{f_a}\right) \tag{1}$$

where 10^{16} GeV $\equiv \Lambda_{\text{GUT}}$ is the grand unification (GUT) scale. An axion of mass $\mathcal{O}(10^{-10})$ eV corresponds to f_a being at the GUT scale. However, as we will see in Sec. VI A, signals in the LSD band are only expected up to ≈32 kHz, corresponding to a 6.6×10^{-11} eV boson.

At boson masses $\mathcal{O}(10^{-11})$ eV, superradiance occurs optimally for BH's with masses between 0.1 and a few solar masses. Subsolar BHs may exist as PBHs [21], and BHs in the $1-4M_\odot$ range might be formed dynamically in binary neutron star mergers [22], accretion-induced collapsing neutron stars [23], or supernovae with unusually high fallback [24,25].

The $1-4M_\odot$ range of BH masses is gradually being populated by microlensing candidates [26] and GW events such as GW190814 [7] and GW230529 [8]. Since the mass distribution for these objects is still unknown, we will limit our attention to stellar-origin BHs with masses between 5 and $20M_\odot$, typical of BHs in x-ray binary systems.

As a first step toward building the LSD search pipeline, we simulate the Galactic population of axion clouds with $5-20M_\odot$ BH hosts. The essential data returned by these simulations are the gravitational-wave frequency and dimensionless strain amplitude emitted by each cloud. Together with the LSD's projected sensitivity curve, we estimate the number of resolvable signals, i.e. those whose signal-to-noise ratio (SNR) rises above a given threshold after a coherent observation time $T_{\text{coh}} = 10^7$ s (a little less than four months). We adopt the idealization of a "freely floating" detector orbiting the Milky Way at the same radius as the Solar System but not situated on a rotating planet orbiting a star. In doing so, we neglect the amplitude and frequency modulations induced by the Earth's sidereal rotation and by its orbital motion in the Solar System. Our results establish a baseline from which a more in-depth analysis, including the aforementioned modulations, can be undertaken in future work.

In Secs. II and III, we introduce the essential physics of axion clouds and their GW emission. To simulate the population of axion clouds, we require a model of the stellar-origin BH population. The parameters of a black hole—mass, spin, age, and location in the Milky Way—are taken to be independent random variables, and we discuss their distributions in Sec. IV. The procedure for determining whether a BH of given mass, spin, and age presently hosts an axion cloud is described in Sec. V. The simulated cloud populations—and the corresponding ensembles of GW signals—are discussed in Sec. VI. Section VII provides a summary of the results, as well as tasks for future work. Throughout the paper, we adopt the metric signature $(-,+,+,+)$, and we retain all factors of G, c, and $\hbar$. We hope our decision not to set physical constants to unity will make this work more accessible to those unaccustomed to the conventions of fundamental physics theory.

II. SUPERRADIANT BOUND-STATES

The creation of macroscopic clouds around spinning black holes can occur for any massive bosonic field. The simplest scenario, the one we adopt, is that of an electrically neutral massive scalar field freely propagating in the Kerr spacetime; we denote the BH mass and dimensionless spin by M and $\chi \equiv Jc/(GM^2)$, respectively (J is the BH angular momentum). We also assume no self-interactions to avoid complications such as the bosenova instability [17]. The scalar field then obeys the Klein-Gordon equation [15],

$$[g^{\mu\nu}\nabla_\mu\nabla_\nu - m_*^2]\Phi(\vec{x},t) = 0 \tag{2}$$

where the constant m_* has dimensions of inverse length; in the quantum theory of a scalar field, the physical meaning of m_* is $1/\lambda_c$, where $\lambda_c \equiv \hbar/(mc) = \hbar c/\mu$ is the reduced

Compton wavelength of the boson, m is the mass of the particle, and $\mu = mc^2$.

In Boyer-Lindquist coordinates, with the ansatz

$$\Phi(\vec{x}, t) = e^{-i\omega t} e^{im\phi} S(\theta) R(r), \tag{3}$$

the Klein-Gordon equation separates into two ordinary differential equations (ODEs) for $R(r)$ and $S(\theta)$. We seek a bound-state solution which is "ingoing" at the event horizon—i.e. a solution which goes to zero at infinity and looks like an ingoing wave at the horizon. The ingoing boundary condition causes the eigenfrequency ω to be complex,

$$\omega = \omega_R + i\omega_I \tag{4}$$

with the consequence that bound-states must either grow or decay

$$e^{-i\omega t} = e^{-i(\omega_R + i\omega_I)t} = e^{-i\omega_R t} e^{\omega_I t}$$

$$\Rightarrow \Phi(\vec{x}, t) = e^{\omega_I t} [e^{-i\omega_R t} e^{im\phi} S(\theta) R(r)]$$

For $\omega_I > 0$, the field amplitude grows exponentially. A necessary and sufficient condition for the growth of a bound-state with azimuthal number m is that the event horizon's angular speed Ω_{H} (times m) be faster than the oscillation of the field [15],

$$\omega_R < m\Omega_{\mathrm{H}}. \tag{5}$$

This requirement is called the "superradiance condition." As the field amplitude grows, the BH loses rotational energy, and Ω_{H} decreases until the inequality becomes an equality. At that point, the superradiant growth ceases, and the resultant bound-state slowly dissipates by emitting GWs.

It is conventional to define a dimensionless "coupling parameter" α as the ratio of the BH's gravitational radius r_g to the reduced Compton wavelength λ_c of the scalar field

$$\alpha \coloneqq \frac{r_g}{\lambda_c} = \frac{GM}{c^2} \frac{\mu}{\hbar c} = \frac{GM\mu}{\hbar c^3}. \tag{6}$$

The "weak-coupling" limit, defined by $\alpha \ll 1$, corresponds to the Compton wavelength of the boson being much larger than the characteristic size r_g of the BH. In this limit, the bound-state energy, given by the real part of ω, can be written in closed form [27]

$$\hbar\omega_R = \mu \left[1 - \frac{\alpha^2}{2n^2} + \left(\frac{2l - 3n + 1}{l + 1/2} - \frac{1}{8} \right) \frac{\alpha^4}{n^4} + \frac{2m\chi\alpha^5}{n^3 l(l + 1/2)(l + 1)} + \cdots \right]. \tag{7}$$

The small "fine-structure" corrections beyond the leading 1 depend on the angular momentum of the cloud and the spin of the BH. The quantity in large square brackets depends on the BH and boson masses only through their dimensionless product α. This motivates the introduction of a dimensionless eigenfrequency $\xi = \xi_R + i\xi_I$

$$\xi_R \equiv \frac{\hbar\omega_R}{\mu} \qquad \xi_I \equiv \frac{\hbar\omega_I}{\mu}. \tag{8}$$

Once we have computed ξ over a sufficiently large region of the (α, χ) parameter space for all bound-states $\{n, l, m\}$ of interest, we can freely plug in any BH masses and axion masses of our choosing. For example, taking $M = 10^7 M_\odot$ and $\mu = 10^{-17}$ eV, we get $\alpha = 0.748$. The same value is obtained taking $M = 10 M_\odot$ and $\mu = 10^{-11}$ eV. The essential consequence is that, for a given BH spin χ, the same set of superradiant bound-states exists for both scenarios.

From a practical point of view, this also means the superradiance condition

$$\xi_R < \frac{m\chi}{2\alpha[1 + \sqrt{1 - \chi^2}]} \equiv \xi_{\mathrm{crit}} \tag{9}$$

becomes a tool for rapidly determining, for a given parameter set $\{\mu, M, \chi\}$, which states are superradiant.

Additionally, far from the BH where relativistic effects are negligible, the radial equation reduces to (r measured in units of λ_c) [16]

$$\left[-\frac{1}{2r^2} \frac{d}{dr} \left(r^2 \frac{d}{dr} \right) - \frac{\alpha}{r} + \frac{l(l+1)}{2r^2} + \frac{1 - \xi^2}{2} \right] R(r) = 0, \tag{10}$$

which is the radial Schrödinger equation for a nonrelativistic particle in a Coulomb potential $V(r) = \alpha/r$, hence the moniker "gravitational atom." The $\alpha^2/(2n^2)$ term in Eq. (7) is precisely the "hydrogen atom" solution to Eq. (10). The complete small-α solutions to the full Klein-Gordon equation have been computed order by order using the method of matched asymptotic expansions [16] (and we have provided an example of Eq. (11) in Figs. 1 and 2),

$$\xi_R = 1 - \frac{\alpha^2}{2n^2} + \left[\frac{2l - 3n + 1}{l + 1/2} - \frac{1}{8} \right] \frac{\alpha^4}{n^4} + \frac{2m\chi\alpha^5}{n^3 l(l + 1/2)(l + 1)} + \cdots, \tag{11}$$

$$\begin{aligned} \xi_I = {} & 2\left(1 + \sqrt{1 - \chi^2}\right) \left[\frac{m\chi}{2\alpha(1 + \sqrt{1 - \chi^2})} - \xi_R \right] \alpha^{4l+5} \\ & \times \frac{2^{4l+1}(n + l)!}{n^{2l+4}(n - l - 1)!} \left(\frac{l!}{(2l)!(2l + 1)} \right)^2 \\ & \times \prod_{j=1}^{l} \left[j^2(1 - \chi^2) + \left[m\chi - 2\alpha\xi_R \left(1 + \sqrt{1 - \chi^2} \right) \right] \right]. \end{aligned} \tag{12}$$

In general, ξ is a function of $\{n,\ l,\ m,\ \alpha,\ \chi\}$. For fixed α and χ, the superradiance rate is largest when

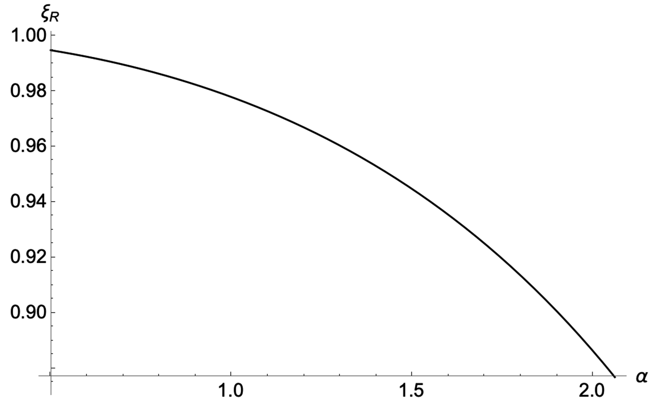

FIG. 1. The real part ξ_R of the $n = 5$ bound-state, for BH spin $\chi = 0.995$, plotted up to the associated maximum superradiant value of the coupling parameter, $\alpha_{\max} = 2.06$.

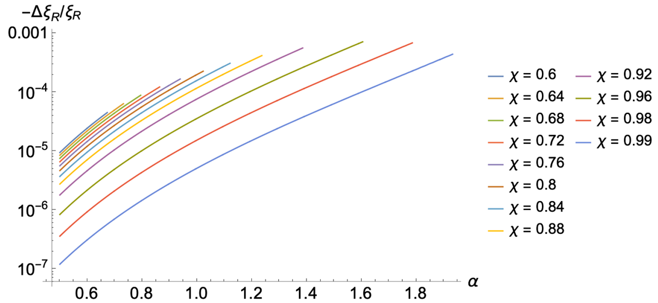

FIG. 2. The ξ_R curve in Fig. 1 corresponds to a BH spin of $\chi = 0.995$. As mentioned in the main text, there are small spin-dependent corrections to ξ_R. Had we plotted several curves in Fig. 1, each corresponding to a different spin, they would lie so close together as to be almost indistinguishable. To spread them out, we plot the fractional deviations between the curve in Fig. 1 and the corresponding curves for a variety of spins. As indicated on the y-axis, the fractional deviations are negative: For a given α, lower BH spin implies lower ξ_R; In turn, this implies a lower GW frequency via Eq. (27).

$m = l = n - 1$. We consider only such bound states in our simulations of the Galactic axion cloud population, reducing the parameter list to $\{n, \chi, \alpha\}$.

Since our fiducial model of the Galactic BH population will assume $M \geq 5M_\odot$, as well as boson masses $\mathcal{O}(10^{-11}\text{–}10^{-10})$ eV, the corresponding values of α are always greater than one but still of order unity. In this "intermediate" regime, there are no closed-form solutions for ξ. As detailed in the Appendix, we must resort to the series-solution method for solving the radial Klein-Gordon equation. The coefficients of the infinite-series ansatz obey a three-term recurrence relation whose solution is equivalent to the solution of a corresponding nonlinear continued-fraction equation [15,28].

Denoting the peak mass of the cloud as M_c, the cloud's growth timescale is given by [29]

$$\tau_c \equiv \tau_{nlm} \ln N = \tau_{nlm} \ln\left(\frac{M_c c^2}{\mu}\right) \tag{13}$$

with N the number of bosons in the cloud and τ_{nlm} the reciprocal of the superradiance rate,

$$\tau_{nlm} \equiv \frac{1}{\Gamma_{nlm}}, \qquad \Gamma_{nlm} \equiv 2\omega_I. \tag{14}$$

τ_{nlm} is the e-folding timescale, and we follow the authors of [29] in taking τ_c as the time to fully grow the bound-state. The factor of two in Γ_{nlm} occurs because the cloud's density is proportional to the 00-component of the stress-energy, $\rho \propto T^0_0 \propto \exp(2\omega_I t)$.

As the cloud grows, the BH gradually loses mass and angular momentum. The growth timescales are long enough to permit an adiabatic treatment of the BH's evolution [30]. The metric can be thought of as Kerr with slowly changing M and χ. Denoting the initial BH parameters as (M_i, χ_i), the cloud's mass is

$$M_c \equiv M_i - M_f \tag{15}$$

and the hole's final mass and spin (M_f, χ_f) are given by [30,31]

$$M_f = M_i\left[\frac{m^3 - \sqrt{m^6 - 16m^2\xi_R^2\alpha_i^2(m - \xi_R\alpha_i\chi_i)^2}}{8\xi_R^2\alpha_i^2(m - \xi_R\alpha_i\chi_i)}\right], \tag{16}$$

$$\chi_f = \left(\frac{M_i}{M_f}\right)^2\left(\chi_i - \frac{mM_c}{\xi_R\alpha_i M_i}\right). \tag{17}$$

Since our simulation of the Galactic axion cloud population requires us to follow the evolution of each BH-cloud system—of which there could be millions—we save computation time by relying on these expressions for the final BH parameters.

The final mass and spin become the new parameters $(M_f \to M_i, \chi_f \to \chi_i)$ for determining which bound-state will grow after the present cloud has dissipated. For our simulations, the superradiance condition [Eq. (9)] is used to determine, from the set $\{1, 2, 3, \ldots\}$, the smallest value of m for which superradiance occurs. The final state of the BH-boson system at the cessation of cloud growth is determined by Eqs. (15)–(17).

III. GRAVITATIONAL WAVES FROM AXION CLOUDS

At a particle-physics level, GW production by axion clouds can be understood in terms of two processes: annihilation of two bosons to a single graviton (with the BH absorbing the recoil momentum) and downward transitions between bound-states [32]. However, just as superradiance is a purely classical kinematic effect, the GW emission can also be understood classically in terms of the cloud's time-dependent quadrupole moment. That being said, the GW signals considered in this work correspond to the annihilation channel.

Since our simulation of the Galactic axion cloud population requires us to compute the GW amplitude for each cloud—of which there could be millions—we save computation time by relying on semianalytic formulas for the amplitudes [31,32]. Following [30], the GW signal seen by a detector with perpendicular arms takes the general form

$$h(t) = F_{+}(t)a_{+}\cos[\Phi(t)] + F_{\times}(t)a_{\times}\sin[\Phi(t)] \tag{18}$$

where $F_{+}(t)$ and $F_{\times}(t)$ are the detector's angular pattern functions, and the phase $\Phi(t)$ encodes the frequency evolution in the detector frame,

$$\begin{aligned}\Phi(t) &= \Phi_0 + 2\pi\int_{T_0}^{T} f(T')dT' \\ &= \Phi_0 + 2\pi\left[f_0(T-T_0) + \frac{1}{2}\dot{f}_0(T-T_0)^2 + \ldots\right],\end{aligned} \tag{19}$$

where $\dot{f}$ is the frequency derivative, quantities with a zero subscript are their values at a reference time T_0, and $T(t)$ is the time at the Solar System barycenter, related to the time at the detector t by the addition of the Rømer, Shapiro, and Einstein delays.

The amplitudes $a_{+/\times}$ are expanded in terms of spheroidal harmonics with spin-weight $s=-2$,

$$a_{+/\times} = -\sum_{\tilde{l}\geq 2l} h_0^{(\tilde{l})}[{}_{-2}S_{\tilde{l},\tilde{m},\tilde{\omega}} \pm {}_{-2}S_{\tilde{l},-\tilde{m},-\tilde{\omega}}], \tag{20}$$

where $\tilde{\omega} = 2\omega_R$ is the GW angular frequency, the parameters (l,m) refer to the scalar bound-state, and $(\tilde{l},\tilde{m})$ refer to the GW modes, with $\tilde{l} \geq 2l$ and $\tilde{m} = 2m$. For each mode, there is a polarization-independent characteristic amplitude $h_0^{(\tilde{l})}$ [30],

$$h_0^{(\tilde{l})} = \frac{c^4}{G}\frac{M_c}{M_f}\frac{1}{2\pi^2 M_f f^2 d}\mathcal{A}_{\tilde{l}\tilde{m}}(\alpha_i,\chi_i), \tag{21}$$

where f is the GW frequency, d is the source distance, and the $\mathcal{A}_{\tilde{l}\tilde{m}}(\alpha,\chi)$ are dimensionless numerical factors which measure how much energy is carried by each mode. The corresponding luminosity in each mode is given by

$$\dot{E}_{\mathrm{GW}}(\tilde{l},\tilde{m},\tilde{\omega}) = \frac{c^5}{4\pi G}\left(\frac{c^3}{GM_f\tilde{\omega}}\right)^2\frac{M_c^2}{M_f^2}\mathcal{A}^2_{\tilde{l}\tilde{m}}(\alpha_i,\chi_i). \tag{22}$$

In principle, the coefficients $\mathcal{A}_{\tilde{l}\tilde{m}}$ must be computed numerically by solving the Teukolsky equation governing linear perturbations of the Kerr metric. The authors of [31] express $\dot{E}_{\mathrm{GW}}$ in the form

$$\dot{E}_{\mathrm{GW}} = \frac{c^5}{G}\frac{M_c^2}{M_f^2}\frac{d\tilde{E}}{dt} \tag{23}$$

and invoke an analytic solution for $d\tilde{E}/dt$, which is formally valid for $\alpha \ll l$ and which remains a good approximation up to $\alpha \sim l$ [32]

$$\frac{d\tilde{E}}{dt} = \frac{16^{l+1}l(2l-1)\Gamma^2(2l-1)\Gamma^2(n+l+1)\alpha_f^{4l+10}}{n^{4l+8}(l+1)\Gamma^4(l+1)\Gamma(4l+3)\Gamma^2(n-l)} \tag{24}$$

where Γ is the gamma function, and α_f denotes the value of α corresponding to the final mass of the BH (i.e. after the cloud has finished growing),

$$\alpha_f = \alpha_i\frac{M_f}{M_i}. \tag{25}$$

Comparing Eqs. (22) and (23), we see that $\mathcal{A}_{\tilde{l}\tilde{m}} \propto \sqrt{d\tilde{E}/dt}$, allowing us to express $h_0^{(\tilde{l})}$ directly in terms of $d\tilde{E}/dt$. Restricting ourselves to the dominant mode $\tilde{m} = \tilde{l} = 2l$, we obtain a closed-form solution for the characteristic amplitude, which we use without abandon to compute the GW amplitudes of the axion clouds resulting from our simulations (we will drop the superscript $(2l)$ henceforth),

$$h_0^{(2l)}(d) = \frac{GM_c}{c^2 d}\frac{2\sqrt{\pi}M_i}{\xi_R\alpha_i M_f}\sqrt{\frac{d\tilde{E}}{dt}}. \tag{26}$$

The corresponding GW frequency is given by

$$f = \frac{\tilde{\omega}}{2\pi} = \frac{1}{2\pi}\frac{2\mu}{\hbar}\xi_R \equiv f_0\xi_R$$

$$f = f_0\xi_R \tag{27}$$

where we've introduced the zeroth-order frequency $f_0 = \omega_0/2\pi$, $\omega_0 \equiv 2\mu/\hbar$.

It is often remarked that the GW frequency is proportional to twice the axion mass, $f \propto 2\mu$. We see that this is, indeed, true in the small-α limit by noting that $\xi_R \to 1$ as $\alpha \to 0$ [Fig. 1, Eq. (11)]. The frequency monotonically decreases with increasing α, and for axion clouds in the kHz band, with stellar-mass BH hosts (where α is generically greater than 1), GW frequencies can be upwards of 10% smaller than the nominal value f_0.

Equation (27) gives the frequency as measured in the rest-frame of the axion cloud. For an observer located elsewhere in the Milky Way, the measured signal is Doppler shifted due to the differential rotation of the Galaxy. We assume all bodies in the Galaxy move in the azimuthal direction, $\vec{v} = v_\phi \hat{\phi}$, and we assume the following Galactic rotation curve [33] (r, in kpc, is the cylindrical radial distance from the Galactic center):

$$v_\phi(r)\ (\mathrm{km/s}) = \begin{cases} 265 - 1875(r-0.2)^2 & r < 0.2 \\ 225 + 15.625(r-1.8)^2 & 0.2 < r < 1.8 \\ 225 + 3.75(r-1.8) & 1.8 < r < 5.8 \\ 240 & r > 5.8. \end{cases} \tag{28}$$

Denoting the source-frame frequency as f_s, the nonrelativistic Doppler-shifted frequency we observe is

$$f_{\mathrm{obs}} = \left(1 - \frac{v_r}{c}\right) f_s, \tag{29}$$

where v_r is the line-of-sight component of the relative velocity between source and observer. v_r is defined to be positive when the source and observer are moving away from each other.

When a cloud finishes growing, it emits GWs whose initial amplitude h_0 is given by Eq. (21). As the cloud dissipates, the amplitude decreases as [29]

$$h(t) = \frac{h_0}{1 + t/\tau_{\mathrm{GW}}}, \tag{30}$$

where τ_{GW} is the time for h to drop to half its initial value.

IV. THE GALACTIC POPULATION OF ISOLATED STELLAR-ORIGIN BLACK HOLES

With the results of the previous sections in hand, we can follow the "superradiance history" of any given BH—i.e. we can determine the sequence of scalar field bound-states, their growth and dissipation timescales, the BH mass and spin decrements, and, above all, the GW frequency and amplitude of each successive cloud. To simulate the entire Galactic population of axion clouds, we must assign each BH a mass, spin, age, and location—taken to be independent random variables—in accordance with known or assumed distributions.

Our knowledge of the stellar-origin BH mass distribution is informed by mass measurements in x-ray binary systems [34–36], microlensing events [37], and astrometry [38], as well as through modeling of the complex physics of core-collapse supernovae [39]. Known BHs typically have masses between $5M_\odot$ and $20M_\odot$, and power-law models are favored when fitting the mass function of low-mass x-ray binaries [34]. Not coincidentally, the massive stars which produce BH remnants are also characterized by a power-law distribution, $\psi(M)dM \propto M^{-2.35}dM$, the "Salpeter" function. We will assume M_{BH} to be Salpeter-distributed on the interval $5 - 20M_\odot$.

BH spins have been measured in several x-ray binaries [40], but none have been measured for isolated BHs. In the case of binaries, the distribution of spin magnitudes is more-or-less uniform, so we take the BH spin to be uniformly distributed, $\chi \sim U[0,1]$.

The stellar content of the Milky Way can be divided into three primary regions—the thin disk, the thick disk, and the central bulge. The age distribution of stellar-origin BHs is tied to the star formation history in each region. As the Milky Way's star formation history is a topic of ongoing research, we take an agnostic approach by assigning each BH an age of 10^x yr, with x uniformly distributed on an interval which varies among the three Galactic regions. For the thin disk and thick disk, we take $x \sim U[3, \log_{10}(8\times10^9)]$ and $x \sim U[3,10]$, respectively [41]. For the bulge, we assign each BH an age 10^x yr, with $x \sim U[9, \log_{10}(13\times10^9)]$ [42].

We assume black holes are distributed in space according to the mass profiles of the disks and bulge described in Ref. [43]. Both disks have the same axisymmetric form, with the corresponding scale lengths, scale heights, and surface densities quoted in Table I

$$\rho_{\mathrm{disk}}(r,z,\phi) = \frac{\Sigma_{\mathrm{d},0}}{2z_{\mathrm{d}}} e^{-|z|/z_{\mathrm{d}}} e^{-r/R_{\mathrm{d}}}. \tag{31}$$

The bulge is also axisymmetric, with the corresponding parameters also given in Table I

$$\rho_{\mathrm{b}} = \frac{\rho_{\mathrm{b},0}}{(1+\frac{r'}{r_0})^\alpha} e^{-(r'/r_{\mathrm{cut}})^2} \tag{32}$$

TABLE I. Physical parameters for the empirical stellar-mass distribution of the Milky Way inferred in Ref. [43]. The values for those with an asterisk (*) are the means marginalized over all other parameters in the model. The disk scale heights are the best-fitting values from Ref. [44], and the stellar bulge model is an axisymmetric modification of the result from Ref. [45] in which the assumption of a constant mass-to-light ratio in the bulge was used to convert photometric data into a mass model.

Disk parameters	Value
$^*R_{\mathrm{d,thin}}$ (kpc)	3.00
$^*R_{\mathrm{d,thick}}$ (kpc)	3.29
$^*\Sigma_{\mathrm{d,0,thin}}$ ($M_\odot \mathrm{pc}^{-2}$)	741
$^*\Sigma_{\mathrm{d,0,thick}}$ ($M_\odot \mathrm{pc}^{-2}$)	238
$z_{\mathrm{d,thin}}$ (kpc)	0.3
$z_{\mathrm{d,thick}}$ (kpc)	0.9
*Solar radius $R_\odot$ (kpc)	8.29
Bulge parameters	Value
*$\rho_{\mathrm{b},0}$ ($M_\odot \mathrm{pc}^{-3}$)	95.5
α	1.8
r_0 (kpc)	0.075
r_{cut} (kpc)	2.1
q	0.5

$$r' \equiv \sqrt{r^2 + (z/q)^2}.$$

We apportion the BHs among the three Galactic regions according to the fractions $f_{\rm thin}$, $f_{\rm thick}$, and $f_{\rm bulge}$, defined by $f_i = M_i/\sum_i M_i$, $i \in \{\text{thin, thick, bulge}\}$. The disk masses are obtained by integrating $\rho_{\rm disk}$, with the radial integral cut-off at 25 kpc and the vertical integral cut-off at 3 scale heights. This gives $3.97 \times 10^{10} M_\odot$ and $1.5 \times 10^{10} M_\odot$ for the thin and thick disks, respectively. We take the bulge mass to be $8.9 \times 10^9 M_\odot$, the value quoted in [43]. The corresponding f_i are 62%, 24%, 14%, respectively. We will assume the Galactic population of $N_{\rm BH}$ BHs to be apportioned likewise: 62% in the thin disk, 24% in the thick disk, and 14% in the bulge.

V. SIMULATION PROCEDURE

The simulation is a procedure by which, for a given axion mass and from an initial population of $N_{\rm BH}$ BHs sprinkled throughout the Milky Way, we determine the number N_c of extant axion clouds. Each simulation outputs the physical properties, distances, and the GW frequencies and amplitudes of the N_c clouds.

At the outset, each BH is assigned a mass, spin, and age. We will illustrate the procedure with an example and then summarize the procedure with a flowchart: taking $\mu = 4 \times 10^{-11}$ eV, consider the evolution of a $5M_\odot$, $\chi = 0.95$ BH with an age of 10^8 yrs. The superradiance condition, Eq. (9), determines which bound-state grows first.

$$\begin{aligned} &\xi_R = 1.03 \quad \xi_{\rm crit} = 0.24 \quad (m = 1)\\ &\xi_R = 0.76 \quad \xi_{\rm crit} = 0.48 \quad (m = 2)\\ &\xi_R = 0.89 \quad \xi_{\rm crit} = 0.73 \quad (m = 3)\\ &\xi_R = 0.94 \quad \xi_{\rm crit} = 0.97 \quad (m = 4) \end{aligned} \tag{33}$$

Since $\xi_R > \xi_{\rm crit}$ for $m = 1$, 2, 3, the first superradiant bound-state is $n = 5$, $l = m = 4$, and it grows on a timescale of $\tau_c = 3.4$ yrs. The BH's mass and spin are decreased to $4.94M_\odot$ and 0.938, respectively. Once the cloud has finished growing, it dissipates on a timescale $\tau_{\rm GW} = 0.8$ yrs. The time from the BH's birth to the cloud's dissipation is only $\tau_c + \tau_{\rm GW} = 4.2$ yrs, leaving plenty of time for new clouds to develop. We denote by t_r the time remaining to the present. In this case, $t_r = 10^8 - 4.2 \approx 10^8$ yrs.

The next bound-state is $n = 6$ with $\tau_c = 3536$ yrs. The BH's mass and spin are decreased to $4.67M_\odot$ and 0.84, respectively. Once the cloud has finished growing, it dissipates on a timescale $\tau_{\rm GW} = 2445$ yrs. At this point, $t_r = 9.9994 \times 10^7$ yrs—still plenty of time left for further superradiance.

The next (and final) bound-state is $n = 7$ with $\tau_c = 6 \times 10^7$ yrs. The BH's mass and spin are decreased to $4.5M_\odot$ and 0.74, respectively. Once the cloud has finished growing, $t_r = 3.9 \times 10^7$ yrs remain. The dissipation timescale $\tau_{\rm GW} = 7 \times 10^7$ yrs. Since $\tau_{\rm GW} > t_r$, the $n = 7$ cloud is still present today. It has an initial mass $M_c = 0.16M_\odot$, and it radiates at $f = 18.9$ kHz. Placing the source at $d = 1$ kpc (for example), the initial strain amplitude $h_0 = 10^{-26}$ [Eq. (26)]. The signal observed today was emitted $d/c = 3300$ yrs ago, so the corresponding amplitude $h(t) = 6.9 \times 10^{-27}$ [Eq. (30) with $t = t_r - d/c$].

Our simulation of the Galactic cloud population consists of applying the foregoing procedure to each of the BHs in the Galaxy. If a given BH only permits a bound-state whose growth timescale is greater than the age of the universe ($\tau_c > \tau_{\rm uni} = 1.38 \times 10^{10}$ yr), the host BH is removed from the simulation.

Our criterion for whether a given cloud is still present today is $\tau_{\rm GW} > t_r$. For each black hole, there are only two final options: either a cloud has finished growing and is still present today, or a cloud is growing on a timescale greater than the age of the universe.

Those BHs with an extant cloud are assigned a location in the Milky Way [Eqs. (31) and (32)]. Earth is assigned to an arbitrary—but fixed—point on the circle of radius 8.3 kpc in the Galactic midplane. For a cloud located at distance d, we check the inequality $ct_r > d$ to determine if there has been enough time for GWs to propagate to Earth since the cloud formed. Those clouds for which $d > ct_r$ are presently unobservable, and we retain only those clouds for which $ct_r > d$. We summarize this section with the following flowchart:

(i) For a given μ, $M_{\rm BH}$, χ, and BH age, find the lowest superradiant value of n.
(ii) If $\tau_c > \tau_{\rm uni}$, the BH is removed from the simulation.
(iii) Otherwise, the dissipation timescale $\tau_{\rm GW}$ determines whether a new cloud will start growing in accordance with $\tau_{\rm GW} > t_r$ (cloud still present) or $\tau_{\rm GW} < t_r$ (cloud has dissipated, and a new cloud begins growing).
(iv) Repeat the previous steps until one of two possibilities is obtained: (a) a cloud is growing with $\tau_c >$ the age of the universe or (b) a cloud is still present and radiating GWs today.
(v) If the cloud hasn't dissipated yet, assign it a random position, and compute the GW strain at Earth's location only if the travel-time inequality $ct_r > d$ is true.

VI. GWS FROM THE AXION CLOUD POPULATION

A. Cloud populations

The total number of stellar-origin black holes has been estimated to be $\mathcal{O}(10^8)$ from the Milky Way's supernova rate of $\mathcal{O}(1)$ century^{-1} [46] and from population-synthesis estimates [47]. We take $N_{\rm BH} = 10^8$, bearing in mind that the true number could be larger by a factor of a few or even another order of magnitude [48]. We have simulated the axion cloud population for $\mu = (3, 3.5, 4, 4.5, 5, 5.5, 6, 6.5) \times 10^{-11}$ eV.

The output of a simulation is a collection of all extant BH-cloud systems in the Milky Way. Those BHs which have experienced the growth of a single cloud are described by a list comprising the BH age, the initial and final values of the BH mass and spin, the bound-state $\{n, l, m, \xi_R, \xi_I\}$, the cloud's properties—mass M_c, growth timescale τ_c, and dissipation timescale τ_{GW}—the source distance d, and the GW frequency and amplitude (f, h). BHs which have experienced the growth of multiple bound-states are each characterized by a set of such lists, one per bound-state. The GW frequency and amplitude are only computed for the extant cloud, all previous bound-states having already dissipated.

For a given axion mass, the number of extant clouds is a random variable whose mean and standard deviation are estimated by performing 20 simulations with 5×10^6 BH's per simulation, computing the sample mean and sample standard deviation of N_c over the 20 trials, and then multiplying them by 20 and $\sqrt{20}$, respectively.

An ensemble of GW signals from axion clouds is a scatter plot in the h vs f plane, as in Figs. 3–5. The distribution of amplitudes and frequencies is not random but consists of well-defined bands corresponding to the various occupied bound-states. The lowest bound-state resulting from our simulations is $n = 6$, reflecting the general difficulty for stellar-mass BHs to produce clouds in the LSD band.

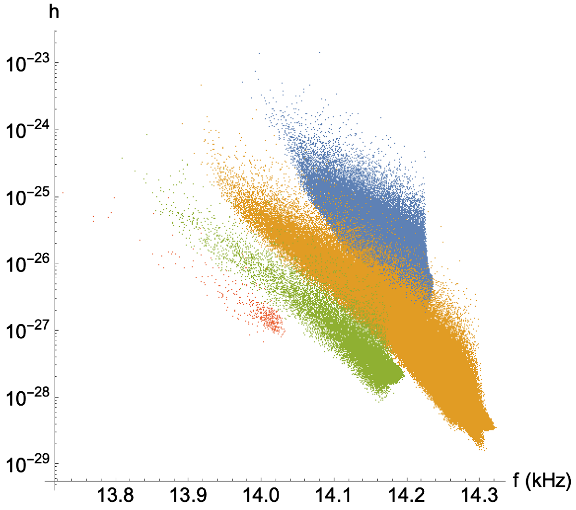

FIG. 3. Population of axion clouds, with $\mu = 3 \times 10^{-11}$ eV. From a population of 10^8 BHs, the simulation returns $N_c = (9.32 \pm 0.03) \times 10^5$ extant clouds. Of these, 8.3×10^5 (89%) satisfy the GW travel-time condition (Sec. V). Since GW amplitudes and frequencies are, necessarily, only computed for those clouds satisfying the travel-time condition, it should be understood that only those clouds are represented in this figure, as well as in Figs. 4 and 5.

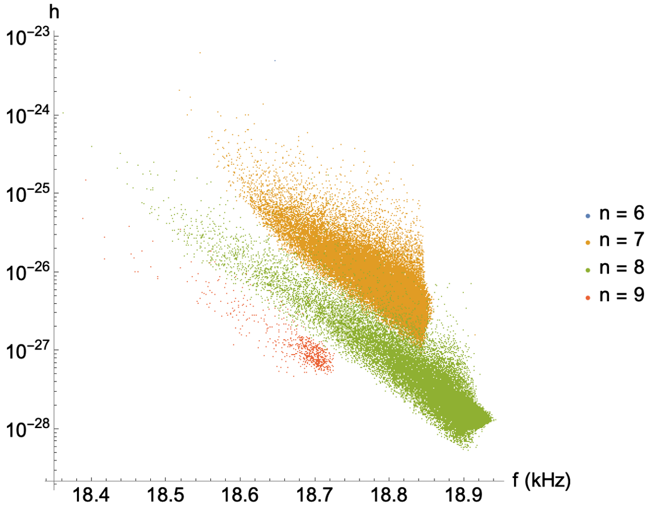

FIG. 4. Population of axion clouds, with $\mu = 4 \times 10^{-11}$ eV. From a population of 10^8 BHs, the simulation returns $N_c = (1.17 \pm 0.01) \times 10^5$ extant clouds. Of these, 9.5×10^4 (81%) satisfy the GW travel-time condition.

Also reflecting this difficulty is the rapid decline in the number of clouds N_c with increasing boson mass μ (Fig. 6). For $\mu = 3 \times 10^{-11}$ eV, $N_c = (9.323 \pm 0.007) \times 10^5$, while at $\mu = 6.5 \times 10^{-11}$ eV, the number has dropped to 130 ± 10. N_c goes to zero around 6.6×10^{-11} eV, corresponding to a nominal upper limit of ≈32 kHz for signals expected in the LSD band. Higher-frequency signals could occur from BHs with $M_{\mathrm{BH}} < 5 M_{\odot}$, especially in light of the recent discoveries of lower-mass-gap objects.

In all cases, the distribution of GW frequencies occurs below the nominal value $f_0 \propto 2\mu$ due to the positive scaling of gravitational redshift with BH mass. This interpretation

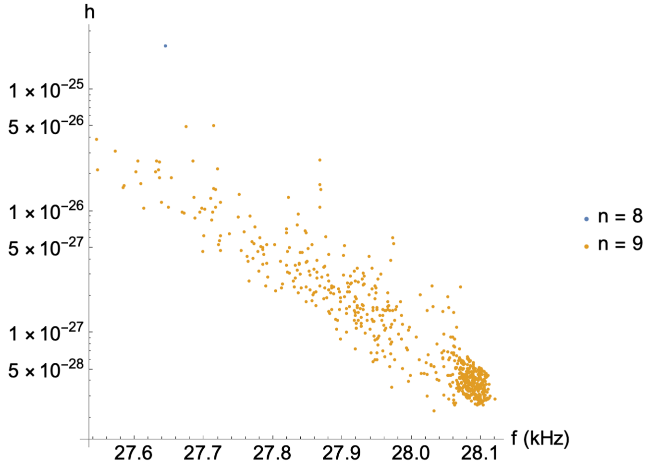

FIG. 5. Population of axion clouds, with $\mu = 6 \times 10^{-11}$ eV. From a population of 10^8 BHs, the simulation returns $N_c = 900 \pm 200$ extant clouds. Of these, 620 (69%) satisfy the GW travel-time condition. The apparent gap in the $n = 9$ band at 28 kHz is an artifact due to the small number of clouds.

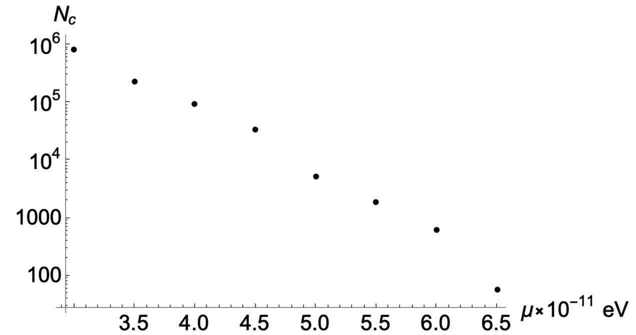

FIG. 6. Number of extant axion clouds N_c drops rapidly with increasing boson mass μ, and it extrapolates to zero around 6.6×10^{-11} eV, corresponding to $f \approx 32$ kHz. In light of the lower-mass-gap objects found by LIGO-Virgo, we note that superradiant instabilities with a $\mathcal{O}(10^{-11})$ eV boson are stronger for $M_{\mathrm{BH}} < 5M_{\odot}$ than for $M_{\mathrm{BH}} > 5M_{\odot}$. Since the BHs involved in our simulations are of the latter type, the true number of clouds, for any boson mass, could be greater than our estimate by a factor depending on the mass distribution and total number of lower-mass-gap BHs in the Milky Way.

is confirmed by a plot of the source-frame GW frequencies $f_{\mathrm{GW,s}}$ and initial BH masses M_i for all extant clouds in a given simulation (Fig. 7, with $\mu = 3 \times 10^{-11}$ eV). For each scalar bound-state, there is a tight relationship, with more massive BHs producing lower-frequency clouds.

In the introduction (Sec. I), we noted a potential connection between the QCD axion and the GUT scale Λ_{GUT} [Eq. (1)]: an axion of mass $\mathcal{O}(10^{-10})$ eV corresponds to $f_a \approx \Lambda_{\mathrm{GUT}}$. If the solution to the strong-CP problem is tied to GUT phenomenology, then discovery of an $\mathcal{O}(10^{-10})$ eV axion would be an exciting, albeit indirect, form of evidence for grand unification. The number of clouds in the Milky Way dropping to zero around 6.6×10^{-11} eV would seem to preclude the possibility of detecting an $\mathcal{O}(10^{-10})$ eV axion—and, by extent, of probing GUT-scale physics with the LSD. Lower-mass-gap BHs could produce clouds at higher μ, thereby reviving hopes of finding a GUT-scale axion. Another possibility is that Λ_{GUT} is model dependent, giving rise to a range of possible values including 10^{17} GeV, which corresponds to $\mathcal{O}(10^{-11})$ eV bosons.

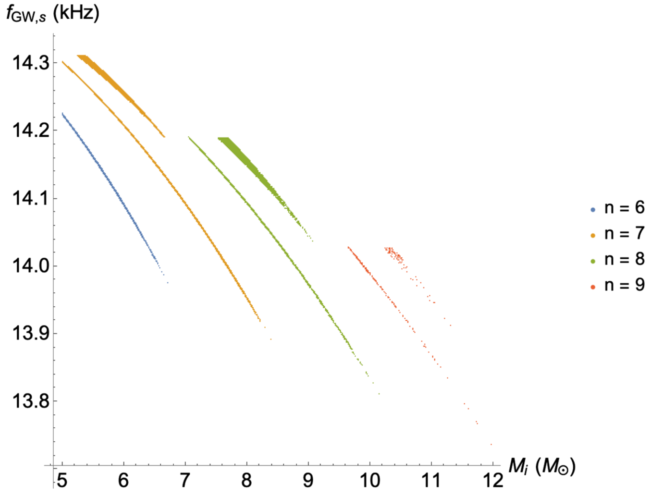

FIG. 7. The source-frame GW frequencies $f_{\mathrm{GW,s}}$ and initial BH masses M_i for the extant clouds in the 3×10^{-11} eV simulation. The distribution of frequencies below the nominal value $f_0 \propto 2\mu$ is a result of gravitational redshift.

B. Resolvable signals

The standard result for coherent detection of a continuous monochromatic signal, $h(t) = h_0 \cos(\omega t)$, is that the signal-to-noise ratio ρ grows as the square-root of the coherent integration time T_{coh} [11]

$$\rho = \frac{h_0 \sqrt{T_{\mathrm{coh}}}}{\sqrt{S_n(f)}} \tag{34}$$

where $\sqrt{S_n(f)}$ is the one-sided amplitude spectral density of the detector noise (the "sensitivity curve") evaluated at the GW frequency, and the trapping frequency of the levitated sensor is constant during the entire observation time. The LSD is an Earth-bound detector for which the observed signal, Eq. (18), experiences both amplitude modulation via the angular dependence of the sensitivity and phase modulation via the Earth's daily (diurnal) rotation and orbital motion. These corrections require knowledge of both the Earth's position and the source position to high accuracy. In an all-sky blind search for axion clouds, the source position is not known ahead of time, so a realistic search will require a large number of templates corresponding to many sky locations. A coherent search for $\mathcal{O}(10)$ kHz GWs over the full observation time ("fully coherent search") of four months is not computationally-feasible because of the need to take fine steps in parameter space. A "semi-coherent" search, in which the observation time is divided into several segments, sacrifices sensitivity for a great reduction in the number of templates needed to perform a coherent search on each segment [49].

As a means of setting upper limits on the expected number of resolvable signals, we compute the SNR for the idealized case of a detector freely orbiting the Milky Way at the same radius as the Solar System (i.e. not attached to a planet or star system). There is a positive frequency derivative due to the gradual dissipation of the cloud which, however, is estimated to be too small to be detected [29]. The signal remains perfectly coherent over the full observation time, and a hypothetical search performed at the Solar System barycenter would simply involve Fourier-transforming the data and looking for lines in the power spectrum.

Taking $T_{\mathrm{coh}} = 10^7$ s—and with the projected sensitivity curves for the current 1 m LSD prototype, as well as for

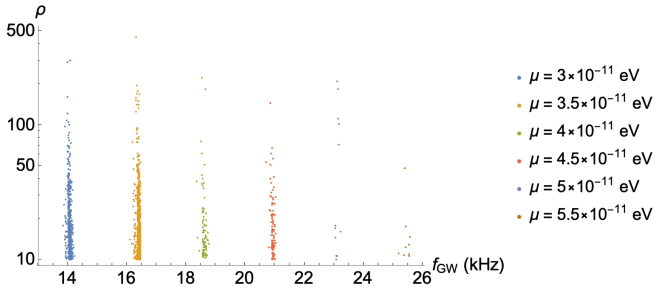

FIG. 8. SNR's ρ of resolvable GW signals from simulated axion cloud populations, for the 100 m LSD. As a function of μ, the number of resolvable signals drops to zero beyond 5.5×10^{-11} eV, thereby constraining the expected frequency range of resolvable sources to $f < 26$ kHz.

future 10 m and 100 m versions [13]—we compute the corresponding SNRs for all sources in the Galaxy. We count those with $\rho > \rho_{\mathrm{t}}$ as resolvable, and we adopt the threshold $\rho_{\mathrm{t}} = 10$ (Fig. 8).

The "loudness" of a signal is determined primarily by the source distance. The distance, in turn, is a random variable determined by the randomly assigned position vector [Eqs. (31) and (32)] of the source. Thus, for a given set of extant clouds, the number of individually resolved sources N_{res} will vary each time we reassign their position vectors. We estimate the mean and standard deviation of N_{res} for a given population of extant clouds by laying them down in the Galaxy $N_{\mathrm{reshuffle}} = 100$ times and counting how many are resolvable in each "reshuffling." The mean and standard deviation are then computed as

$$\bar{N}_{\mathrm{res}} = \frac{1}{N_{\mathrm{reshuffle}}} \sum_{i=1}^{N_{\mathrm{reshuffle}}} N_{\mathrm{res},i}, \tag{35}$$

$$\bar{\sigma}_{\mathrm{res}} = \frac{1}{N_{\mathrm{reshuffle}} - 1} \sum_{i=1}^{N_{\mathrm{reshuffle}}} (N_{\mathrm{res},i} - \bar{N}_{\mathrm{res}})^2. \tag{36}$$

With a 100 m detector, assuming $\mu = 3 \times 10^{-11}$ eV, $\bar{N}_{\mathrm{res}} = 600$ with $\bar{\sigma}_{\mathrm{res}} = 20$. In the most pessimistic case ($\mu = 5.5 \times 10^{-11}$ eV), there are only $\mathcal{O}(1)$ resolvable signals, and we have not estimated the associated uncertainty. The 10–26 kHz range is where we expect resolvable signals to be present for a 100 m LSD. For a 10 m instrument, $\mathcal{O}(1)$ resolvable signals appear at $\mu = 3 \times 10^{-11}$ eV, while a 1 m instrument does not have the required sensitivity to detect individual sources.

In the event a continuous monochromatic signal is detected by the LSD, we will have to answer the question: is this signal from an "axion cloud"—a superradiant bound-state of a scalar (spin-0) field—or from a cloud involving a spin-1 ("Proca") field? In general, Proca fields give rise to stronger GW signals than scalar fields [50]. As a result, we would expect resolvable signals from Proca clouds to be found at greater distances than those from scalar clouds. For the 100 m detector, with $\mu = 3 \times 10^{-11}$ eV, the resolvable signals are depicted in terms of their SNRs and source distances in Fig. 9. The vast majority are less than 3 kpc away. Turning this on its head, the detection of a continuous monochromatic signal with an inferred distance significantly greater than 3 kpc could be a potential indicator of a spin-1 field.

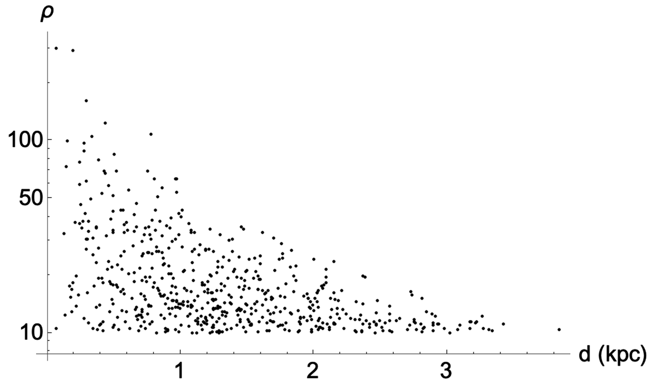

FIG. 9. Scatter plot of the SNR's ρ and source distances d of resolvable signals for the 100 m LSD, taking $\mu = 3 \times 10^{-11}$ eV. There appears to be an upper limit $d \lesssim 3$ kpc and certainly a hard upper limit $d < 4$ kpc, suggesting a way to distinguish between spin-0 and spin-1 bosonic clouds: Proca clouds are generally louder GW sources than axion clouds, so a GW signal with $d \gg 3$ kpc could be taken as evidence of a spin-1 field.

C. Unresolved signals

For all boson masses, the majority of GW signals have amplitudes less than 10^{-23}, with the weakest having $h = \mathcal{O}(10^{-29})$. The unresolvable signals incoherently combine to form a Galactic confusion foreground which manifests as an excess noise in the detector. As before, we neglect the diurnal and annual modulations of the background and instead provide a preliminary estimate of the foreground's strength compared to the nominal 1 m, 10 m, and 100 m LSD sensitivity curves. In a strain-frequency plot (e.g. Fig. 3), we bin the cloud amplitudes [with bin width $\delta f = 10^{-2} f_c$, where f_c is the center frequency of a given bin, and the factor 10^{-2} is the full-width-at-half-maximum (FWHM) of the trapped object's response function around f_c], and we associate an rms amplitude, defined as follows, with each bin.

We start by creating a bin centered on the frequency of the cloud with the smallest GW frequency in a strain-frequency plot, e.g. Fig. 3. All axion clouds emit monochromatic signals,

$$h_i(t) = h_{0,i} \cos(2\pi f t + \phi_i), \tag{37}$$

where the phases ϕ_i are uniformly distributed between 0 and 2π, and i runs over all clouds in the bin. The squared sum of all signals in the bin is time-averaged over a period $T_c = 1/f_c$, where f_c is the frequency at the center of the bin; the result is a dimensionless time-averaged power associated with that bin. The square root of the power represents an effective amplitude $h_{\rm eff}$ of the confusion foreground in the bin,

$$h_{\rm eff} \coloneqq \sqrt{\frac{1}{T_c}\int_0^{T_c} dt \left[\sum_i h_i(t)\right]^2}. \tag{38}$$

We then create a new bin with center frequency $f_c|_{\rm new}$ and width $\delta f|_{\rm new}$,

$$f_c|_{\rm new} = f_c|_{\rm old} + 10^{-2}\delta f|_{\rm old}, \tag{39}$$

$$\delta f|_{\rm new} = 10^{-2} f_c|_{\rm new}, \tag{40}$$

and we compute $h_{\rm eff}$ for this bin. The center frequency is shifted rightwards by a fraction (arbitrarily chosen to be 10^{-2}) of the previous bin width so that adjacent bins overlap, ensuring some degree of continuity in $h_{\rm eff}$ vs f. We continue until we reach the rightmost end of the cloud population. Each bin is then characterized by an ordered pair $(f_c, h_{\rm eff})$ (Fig. 10).

A preliminary method for estimating the LSD's sensitivity to the confusion foreground is to treat each pair $(f_c, h_{\rm eff})$ as if they were the frequency and amplitude of a hypothetical monochromatic signal whose corresponding effective SNR $\rho_{\rm eff}$, computed via Eq. (34), is then compared to a threshold $\rho_{\rm t}$. We continue to require $\rho_{\rm t} = 10$. The numerator and denominator of Eq. (34) ($h_{\rm eff}\sqrt{T_{\rm coh}}$ and

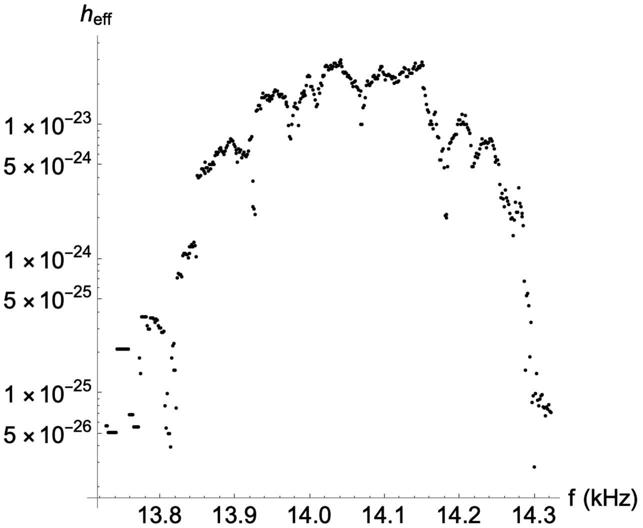

FIG. 10. Effective amplitudes $h_{\rm eff}$, as defined in Eq. (38), for the binned GW amplitudes of a simulated population of axion clouds with $\mu = 3\times10^{-11}$ eV. The width of each bin is a factor 10^{-2} of the central frequency f_c, reflecting the FWHM of the detector response when the trap frequency is f_c.

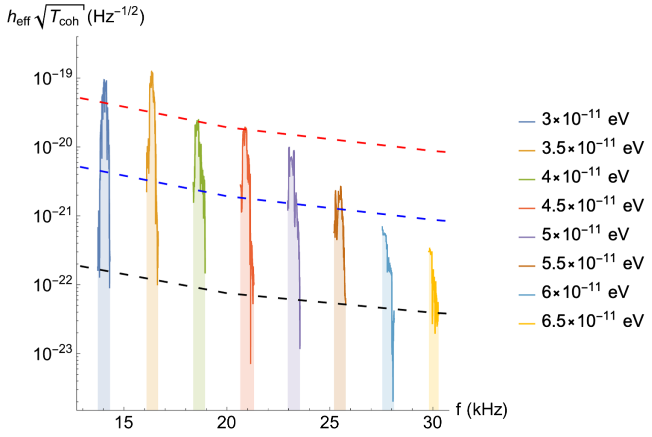

FIG. 11. Confusion-limited foreground of unresolved axion clouds, as a function of the boson mass μ, taking $T_{\rm coh} = 10^7$ s. The 1, 10, and 100 m LSD sensitivity curves are depicted by the red, blue, and black dashed curves, respectively.

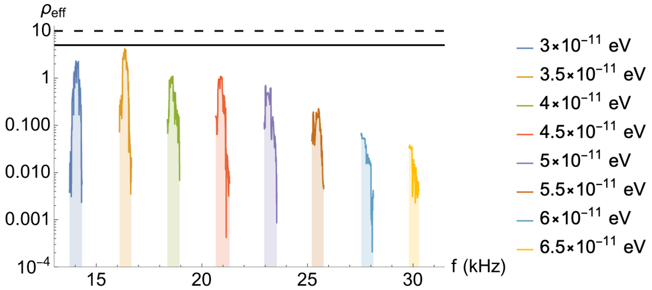

FIG. 12. Corresponding SNR $\rho_{\rm eff}$ of the confusion-limited foreground with respect to the 1 m LSD sensitivity curve. The dashed line depicts the detection threshold $\rho_t = 10$ adopted in this paper, and the solid line represents a lower threshold of five. The foreground does not rise above either threshold.

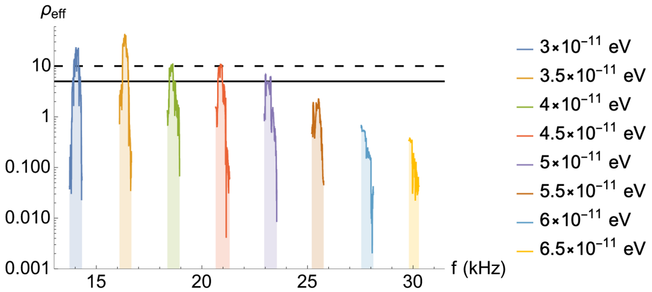

FIG. 13. Corresponding SNR $\rho_{\rm eff}$ of the confusion-limited foreground with respect to the 10 m LSD sensitivity curve. The dashed line depicts the detection threshold $\rho_t = 10$ adopted in this paper, and the solid line represents a lower threshold of five. Over an observation time of 10^7 s, the 10 m instrument has the required sensitivity to detect the foreground in the range $(3\text{–}4.5)\times10^{-11}$ eV, although in the $(4\text{–}4.5)\times10^{-11}$ eV range, only the peak rises above the threshold—and only barely so. If a lower threshold $\rho_t = 5$ were adopted, the range of boson masses could be extended up to 5×10^{-11} eV.

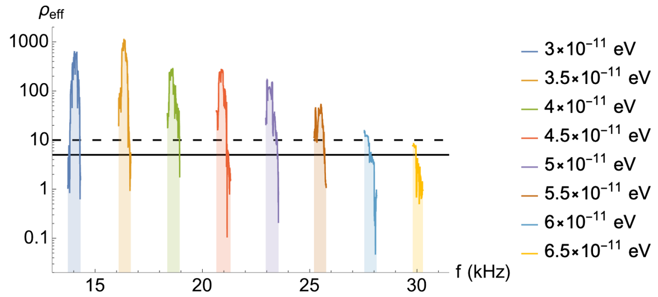

FIG. 14. Corresponding SNR ρ_{eff} of the confusion-limited foreground with respect to the 100 m LSD sensitivity curve. The dashed line depicts the detection threshold $\rho_t = 10$ adopted in this paper, and the solid line represents a lower threshold of five. In the (3–6) $\times 10^{-11}$ eV range, the foreground is predicted to be detectable by a 100 m instrument with effective SNRs upwards of a thousand in the (3–3.5) $\times 10^{-11}$ eV range.

$\sqrt{S_n(f_c)}$, respectively) are shown separately in Fig. 11, and their ratio (the SNR) is shown in Figs. 12–14 for the 1, 10, and 10 m instruments, respectively.

We find that a single 1 m LSD does not appear to have the required sensitivity to detect the foreground for any value of μ. A 10 m detector could detect the foreground with $\rho_{\mathrm{eff}} = \mathcal{O}(10)$ if the axion mass $\mu \in (3\text{–}4) \times 10^{-11}$ eV, while in the (4–4.5) $\times 10^{-11}$ eV range, only the peak of the foreground rises to the threshold—and just barely so (Fig. 13). A 100 m instrument could detect the foreground with large ρ_{eff} if $\mu \in (3\text{–}6) \times 10^{-11}$ eV (Fig. 14). In the range (3–3.5) $\times 10^{-11}$ eV, the peak value of ρ_{eff} is $\mathcal{O}(10^3)$ and remains $\mathcal{O}(10^2)$ up to 5×10^{-11} eV.

VII. CONCLUSION

We have produced Galactic-scale populations of the hypothetical GW sources known as "axion clouds" with the axion mass chosen to correspond to frequencies in the 10–100 kHz band. By computing superradiant bound-states up to $n = 9$, we have accounted for nearly all clouds with growth timescales less than the age of the universe.

The largest number of clouds occurs for the lightest boson mass capable of producing GWs at the frequencies of interest. This was to be expected, as superradiance occurs more readily for small $\alpha \propto \mu M_{\mathrm{BH}}$. For a BH of mass $M \geq 5 M_{\odot}$, the smallest value of α is obtained with the smallest allowed boson mass, 3×10^{-11} eV. In this most optimistic case, the total number of extant clouds is close to 1×106.

The population of axion clouds has been assumed to be spatially distributed within the Milky Way in the same way as the stellar disks and central bulge. Statistically, some may be near enough that the continuous monochromatic signal can be detected by observing over a long enough period of time, e.g. 10^7 s, such that the SNR rises above a given threshold ρ_{t}. We have imposed a stringent threshold $\rho_{\mathrm{t}} = 10$, but we leave it for future work to determine the most appropriate threshold for our search pipeline. For a 100 m instrument, several hundred resolvable signals are predicted to occur if $\mu \approx 3 \times 10^{-11}$ eV, but this number could be upwards of an order of magnitude larger if the total number of stellar-origin BHs is also larger than we have assumed (see the comment made at the beginning of Sec. VI). For a 10 m detector, only $\mathcal{O}(1)$ resolvable signals occur in our simulation at $\mu = 3 \times 10^{-11}$ eV.

Meanwhile, the ensemble of unresolved signals produces a confusion foreground which is estimated to be detectable with potentially large SNR by a 100 m LSD—assuming $\mu \in (3\text{–}6) \times 10^{-11}$ eV—or by a 10 m instrument at moderate SNR, assuming $\mu \in (3\text{–}4.5) \times 10^{-11}$ eV.

Finally, we note the following limitations of this work, as well as directions for future work. First, since isolated BH's have no EM counterpart, we do not know, ahead of time, the direction to these GW sources. Targeted and directed searches for axion clouds will, therefore, not be possible for isolated BHs, and we must resort to blind all-sky searches. Doppler modulations of the GW frequency can be accounted for by including the source's right ascension and declination as additional parameters in the signal model for Bayesian parameter estimation. To avoid the number of demodulation templates becoming prohibitively large—we do not want the time required for data analysis to be greater than the four-month observation period—we will resort to semicoherent techniques for constructing a detection statistic. A final complication might be that a source has a transverse proper motion large enough to change its sky location within the observation time.

In this work, we have used the SNR as a baseline detection statistic. Since we have not yet developed the full semicoherent search pipeline, we do not yet know what is the most appropriate detection statistic for continuous monochromatic signals. Another outstanding question pertains to our scan strategy: given that we will take data at each trapping frequency for 4 months, how finely should the set of frequencies be discretized? At what frequency should we begin our searches? Figs. 8 and 11 both indicate the 14–20 kHz range to be the most optimistic, in terms of the expected number of resolvable signals and the strength of the confusion foreground, respectively.

Additionally, our treatment of the confusion foreground has not accounted for the intrinsic anisotropy of the signal: the axion clouds will be distributed throughout the disks and bulge of the Milky Way, so the strength of the foreground will vary over the sky in a complicated way. Searches for stochastic signals typically involve an "excess-power" method, as well as cross-correlation between multiple detectors. Plans to build a second 1 m instrument at UC Davis (in addition to the Northwestern detector) are in development, so while a single 1 m detector might not have the requisite sensitivity, the prospects for a two- or multi-detector scheme are an exciting avenue of future study.

ACKNOWLEDGMENTS

We would like to thank Vedant Dhruv for making public his *Mathematica* notebook for scalar bound-states in Kerr. We also thank Timothy Kovachy for clarifying issues of numerical precision when using *Mathematica*'s root-finding routines and Richard Brito for several clarifying discussions on axion clouds and their gravitational-wave emission. J. S., A. G., and S. L. are supported by the W. M. Keck Foundation. A. G., G. W., and N. A. are supported in part by NSF grants PHY-2110524 and PHY-2111544, the Heising-Simons Foundation, the John Templeton Foundation, and ONR Grant No. N00014-18-1-2370. N. A. is partially supported by the CIERA Postdoctoral Fellowship from the Center for Interdisciplinary Exploration and Research in Astrophysics at Northwestern University and the University of California, Davis. S. L. is also supported by EPSRC International Quantum Technologies Network Grant No. EP/W02683X/1 and is grateful for EPSRC support through Standard Research Studentship (DTP) EP/R51312X/1. V. K. is supported by a CIFAR Senior Fellowship and through Northwestern University through the D. I. Linzer Distinguished University Professorship. A. L. is supported by the Fannie and John Hertz Foundation. This work used the Quest computing facility at Northwestern.

DATA AVAILABILITY

No data were created or analyzed beyond what is included in this article.

APPENDIX: SUPERRADIANT BOUND-STATES

The creation of an axion cloud corresponds to an instability of the Kerr space-time due to the presence of a massive scalar field. The amplifying mechanism, "superradiance," is the Penrose process in which rotational energy is extracted by a bosonic wave rather than by a particle. In the process, the Kerr BH loses mass and angular momentum, subject to the condition that its "irreducible mass" does not decrease.

In the Penrose scenario, a particle travelling through a BH's ergoregion can split in two, one of which falls into the hole, while the other escapes to infinity. If the orbital angular momentum of the infalling particle is of opposite sign to that of the hole, the BH loses rotational energy to the escaping particle: energy has been extracted from the ergoregion.

The story for waves runs analogously: an incident wave with amplitude $\mathcal{I}$ splits into a part transmitted into the BH (with amplitude $\mathcal{T}$) and a part which escapes (the reflected wave with amplitude $\mathcal{R}$). If the transmitted wave is counterrotating, the rotational energy of the BH decreases, leading to an outgoing wave with $\mathcal{R} > \mathcal{I}$.

The novelty of a massive scalar field is that its mass acts like a mirror: unlike a massless field, a massive field can become trapped in a bound-orbit, leading to continuous extraction of rotational energy. The end result of the runaway amplification is a macroscopic scalar field bound-state—the "axion cloud." In an astrophysical context, rather than a wave incoming from infinity, the initial seed for superradiance can be any arbitrary quantum fluctuation in the scalar field, even if the field is in its classical ground state [29,30]. As a result, the growth of an axion cloud begins immediately after the birth of a BH.

An axion cloud's binding energy (which determines the GW frequency) and growth timescale depend on the dynamics of the scalar field. For the scenario we have adopted, the field obeys the Klein-Gordon equation on the Kerr space-time. The Kerr metric describes an axisymmetric, neutral, and rotating black hole

$$\begin{aligned} ds^2 = -\left[1-\frac{2GMr}{c^2\rho^2}\right]c^2dt^2 - \frac{4GMar\sin^2\theta}{c^2\rho^2}c\,dt\,d\phi \\ +\frac{\rho^2}{\Delta}dr^2 + \rho^2 d\theta^2 + \left[r^2+a^2+\frac{2GMa^2r\sin^2\theta}{c^2\rho^2}\right] \\ \times \sin^2\theta\, d\phi^2 \end{aligned} \tag{A1}$$

where M is the BH mass, J is the BH angular momentum, $\rho^2 \equiv r^2 + a^2\cos^2\theta$, $a \equiv J/(Mc)$ is the Kerr parameter, and $\Delta \equiv r^2 - 2r_g r + a^2$, where we have defined the gravitational radius $r_g \equiv GM/c^2$. In terms of the dimensionless Kerr parameter, $\chi \equiv a/r_g = Jc/(GM^2)$, the inner and outer horizons—the two roots of $\Delta = (r - r_+)(r - r_-)$—are

$$r_\pm = r_g\left[1 \pm \sqrt{1-\chi^2}\right]. \tag{A2}$$

It follows that χ is restricted to the interval

$$0 < \chi < 1. \tag{A3}$$

The event horizon is located at $r = r_+$, and the angular velocity of the horizon is

$$\Omega_H = \frac{c\chi}{2r_+}. \tag{A4}$$

The scalar field obeys the Klein-Gordon equation,

$$[\nabla_\mu\nabla^\mu - m_*^2]\Phi(\vec{x}, t) = 0, \tag{A5}$$

where ∇_μ is the covariant derivative with respect to the Kerr metric, and, as mentioned in the text, m_* has the quantum-mechanical interpretation as the reciprocal of the boson's Compton wavelength. In Boyer-Lindquist coordinates, the Klein-Gordon equation is separable via the ansatz

$$\Phi(\vec{x},t) = \mathrm{Re}[e^{-i\omega t}e^{im\phi}S(\theta)R(r)]. \tag{A6}$$

Invoking the identity

$$\nabla_\mu\nabla^\mu\Phi = \frac{1}{\sqrt{-g}}\partial_\mu[\sqrt{-g}g^{\mu\nu}\partial_\nu\Phi] \tag{A7}$$

$$\sqrt{-g} = \rho^2\sin\theta$$

the Klein-Gordon equation separates into two second-order linear homogeneous ODEs for $R(r)$ and $S(\theta)$

$$\mathcal{D}_\theta[S] + \left[\chi^2\alpha^2(\xi^2-1)\cos^2\theta - \frac{m^2}{\sin^2\theta} + \Lambda\right]S(\theta) = 0, \tag{A8}$$

$$\begin{aligned}&\mathcal{D}_r[R] + [\alpha^2\xi^2(r^2+\chi^2)^2 - 4\chi m\alpha\xi r + m^2\chi^2 \\ &\quad - \Delta(\alpha^2r^2 + \chi^2\alpha^2\xi^2 + \Lambda)]R(r) = 0,\end{aligned} \tag{A9}$$

$$\mathcal{D}_\theta \equiv \frac{1}{\sin\theta}\frac{d}{d\theta}\left[\sin\theta\frac{d}{d\theta}\right], \qquad \mathcal{D}_r \equiv \Delta\frac{d}{dr}\left[\Delta\frac{d}{dr}\right]. \tag{A10}$$

We have expressed the decoupled equations in terms of the dimensionless variables (χ, α, and ξ) used in the main text. The radial coordinate in (A9) is measured in units of r_g.

Bound-state solutions must go to zero at infinity and be ingoing at the event horizon. The ingoing condition means that $R(r) \propto e^{-ikr_*}$ as $r_* \to -\infty$, with r_* the Kerr tortoise coordinate which maps the event horizon to $-\infty$,

$$\frac{dr_*}{dr} = \frac{r^2+a^2}{\Delta}. \tag{A11}$$

This means that plane waves at the event horizon ($r_* \to -\infty$) can only move "to the left," i.e. into the black hole.

The spectra of both bound-states and BH quasinormal modes can be found via Leaver's continued-fraction method [51,15]. The radial function $R(r)$ is represented by an infinite series,

$$R(r) = (r-r_+)^{-i\sigma}(r-r_-)^{i\sigma+\beta-1}e^{qr}\sum_{n=0}^{\infty}a_n\left(\frac{r-r_+}{r-r_-}\right)^n, \tag{A12}$$

$$\sigma = \frac{\alpha(1+\sqrt{1-\chi^2})(\xi-\xi_{\mathrm{crit}})}{\sqrt{1-\chi^2}}, \tag{A13}$$

$$q = \alpha\sqrt{1-\xi^2}, \tag{A14}$$

$$\beta = \frac{\alpha^2(1-2\xi^2)}{q}. \tag{A15}$$

(The quantity we denote by β is the same as the quantity denoted by χ in Ref. [15].) With this ansatz, (A9) implies a three-term recurrence relation for the unknown coefficients a_n,

$$\begin{aligned}&\alpha_n a_{n+1} + \beta_n a_n + \gamma_n a_{n-1} = 0, \quad n = 1,2,\ldots \\ &a_1 = -\tfrac{\beta_0}{\alpha_0}a_0,\end{aligned} \tag{A16}$$

where the coefficients α_n, β_n, and γ_n are defined by

$$\begin{aligned}\alpha_n &= n^2 + (c_0+1)n + c_0 \\ \beta_n &= -2n^2 + (c_1+2) + c_3 \\ \gamma_n &= n^2 + (c_2-3)n + c_4\end{aligned} \tag{A17}$$

and c_0, c_1, c_2, c_3, and c_4 are given by

$$c_0 = 1 - 2i\alpha\xi - \frac{2i(\alpha\xi - \frac{m\chi}{2})}{\sqrt{1-\chi^2}}, \tag{A18}$$

$$\begin{aligned}c_1 = &-4 + 4i\left[\alpha\xi - i\alpha\sqrt{1-\xi^2}\left(1+\sqrt{1-\chi^2}\right)\right] \\ &+ \frac{4i(\alpha\xi - \frac{m\chi}{2})}{\sqrt{1-\chi^2}} - \frac{2[\alpha^2\xi^2 + \alpha^2(1-\xi^2)]}{\alpha\sqrt{1-\xi^2}},\end{aligned} \tag{A19}$$

$$c_2 = 3 - 2i\alpha\xi - \frac{2[\alpha^2(1-\xi^2) - \alpha^2\xi^2]}{\alpha\sqrt{1-\xi^2}} - \frac{2i(\alpha\xi - \frac{m\chi}{2})}{\sqrt{1-\chi^2}}, \tag{A20}$$

$$\begin{aligned}c_3 = &\frac{2i(\alpha\xi - i\alpha\sqrt{1-\xi^2})^3}{\alpha\sqrt{1-\xi^2}} + \chi^2\alpha^2(1-\xi^2) \\ &- \Lambda_{lm} - 1 + 2\sqrt{1-\chi^2}\left(\alpha\xi - i\alpha\sqrt{1-\xi^2}\right)^2 \\ &+ 2im\chi\alpha\sqrt{1-\xi^2} - \frac{\left(\alpha\xi - i\alpha\sqrt{1-\xi^2}\right)^2}{\alpha\sqrt{1-\xi^2}} \\ &+ 2\alpha\sqrt{1-\xi^2}\sqrt{1-\chi^2} \\ &+ \frac{2i}{\sqrt{1-\chi^2}}\left[1 + \frac{(\alpha\xi - i\alpha\sqrt{1-\xi^2})^2}{\alpha\sqrt{1-\xi^2}}\right]\left[\alpha\xi - \frac{m\chi}{2}\right],\end{aligned} \tag{A21}$$

$$\begin{aligned}c_4 = &\frac{\left(\alpha\xi - i\alpha\sqrt{1-\xi^2}\right)^4}{\alpha^2(1-\xi^2)} + \frac{2i\xi\left(\alpha\xi - i\alpha\sqrt{1-\xi^2}\right)^2}{\sqrt{1-\xi^2}} \\ &- \frac{2i\left(\alpha\xi - i\alpha\sqrt{1-\xi^2}\right)^2(\alpha\xi - \frac{m\chi}{2})}{\alpha\sqrt{1-\xi^2}\sqrt{1-\chi^2}}.\end{aligned} \tag{A22}$$

The series coefficients are related by an infinite continued fraction [28]

$$\frac{a_{n+1}}{a_n} = -\frac{\gamma_{n+1}}{\beta_{n+1} - \frac{\alpha_{n+1}\gamma_{n+2}}{\beta_{n+2}-\ldots}}. \tag{A23}$$

Continued fractions are commonly written in the slightly less cumbersome notation

$$\frac{a_{n+1}}{a_n} = -\frac{\gamma_{n+1}}{\beta_{n+1}-}\,\frac{\alpha_{n+1}\gamma_{n+2}}{\beta_{n+2}-}\,\frac{\alpha_{n+2}\gamma_{n+3}}{\beta_{n+3}-}\ldots. \tag{A24}$$

Since $a_1/a_0 = -\beta_0/\alpha_0$, we obtain a condition whose roots are the desired bound-state frequencies

$$\beta_0 - \frac{\alpha_0\gamma_1}{\beta_1-}\,\frac{\alpha_1\gamma_2}{\beta_2-}\,\frac{\alpha_2\gamma_3}{\beta_3-}\ldots = 0. \tag{A25}$$

Strictly speaking, the radial and angular eigenvalues, ξ and Λ, must be found simultaneously. Leaver's method can also be applied to (A8) [52], resulting in a continued-fraction condition analogous to (A25). We then have two equations for the two unknowns.

Conveniently, we can reduce the root-finding problem to merely solving (A25) by using the *Mathematica* function SpheroidalEigenvalue. With the change of variable $z = \cos\theta$—and in terms of the following quantities:

$$\gamma^2 \equiv \chi^2\alpha^2(1-\xi^2), \tag{A26}$$

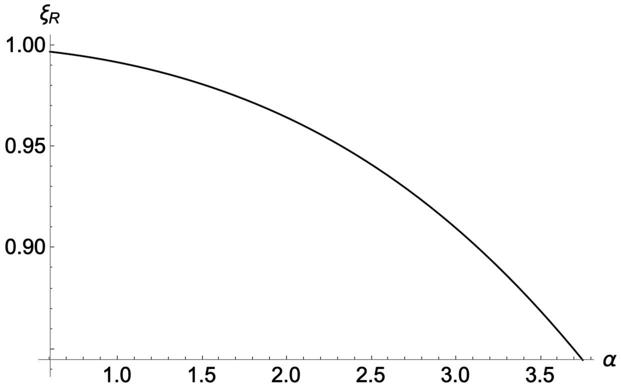

FIG. 15. Real part ξ_R of the $n = 8$ bound-state, for BH spin $\chi = 0.995$, plotted up to the associated maximum superradiant value of the coupling parameter, $\alpha_{\max} = 3.75$.

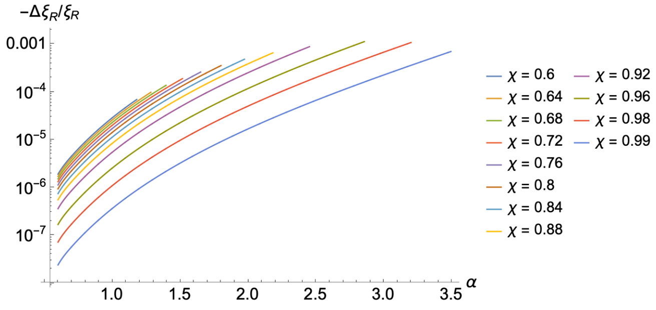

FIG. 16. Fractional deviations between Fig. 15 and the ξ_R curves for various other spins.

$$\lambda \equiv \Lambda - \gamma^2, \tag{A27}$$

the angular equation (A8) takes the standard form implemented in *Mathematica*

$$(1-z^2)\frac{d^2S}{dz^2} - 2z\frac{dS}{dz} + \left[\gamma^2(1-z^2) + \lambda - \frac{m^2}{1-z^2}\right]S(z) = 0. \tag{A28}$$

SpheroidalEigenvalue yields λ, and SpheroidalPS yields $S(z)$. The continued-fraction equation (A25), with Λ replaced by $\gamma^2 +$ SpheroidalEigenvalue, can then be solved for ξ with the *Mathematica* function FindRoot.

For our axion cloud simulations, we have needed to compute ξ for bound-states up to (and including) $n = 9$. As an example, we have plotted the real and imaginary parts of the $n = 8$ bound-state in Figs. 15–17; Figs. 15 and 16 are analogous to Figs. 1 and 2.

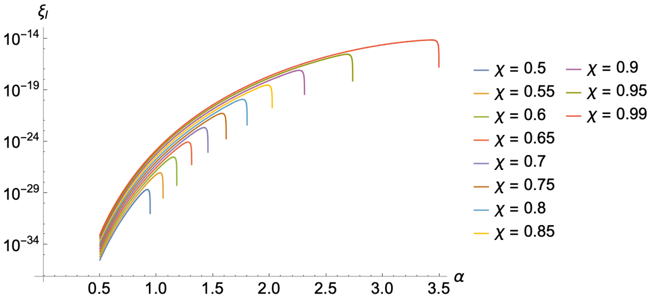

FIG. 17. Imaginary part of the $n = 8$ bound-state eigenfrequency.

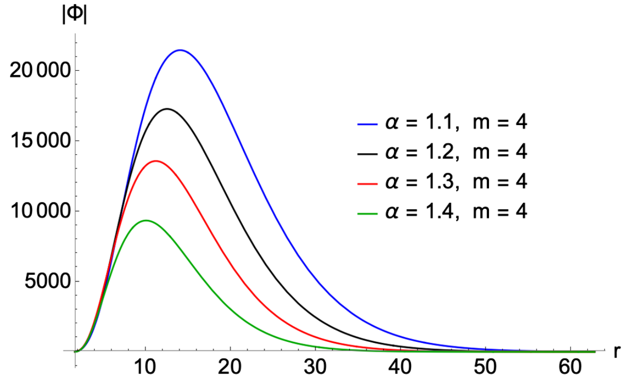

FIG. 18. Radial profiles $|\Phi(r; t = 0, \theta = \pi/2, \phi = 0)|$ of the $n = 5$, $l = m = 4$ superradiant bound-state for a BH of spin $\chi = 0.99$ at four consecutive values of α. The peak of the axion cloud shifts toward the BH with increasing α. This makes sense by comparison with the hydrogen atom: for the $l = n - 1$ states of the hydrogen atom, the most probable radius r_{mp} is inversely proportional to the electromagnetic fine-structure constant α_{EM}: $r_{\mathrm{mp}} = n^2 a_{\mathrm{B}} \propto n^2/\alpha_{\mathrm{EM}}$, where a_{B} is the Bohr radius. While α_{EM} is actually a constant, the analog for scalar field bound-states in Kerr, $\alpha \propto \mu M$, is different for each BH. As a result, for fixed n, the most probable radius for the $l = n - 1$ bound-states decreases with α.

[1] B. P. Abbott (LIGO Scientific and Virgo Collaborations), GWTC-1: A gravitational-wave transient catalog of compact binary mergers observed by LIGO and Virgo during the first and second observing runs, Phys. Rev. X **9**, 031040 (2019).

[2] R. Abbott (LIGO Scientific and Virgo Collaborations), GWTC-2: Compact binary coalescences observed by LIGO and Virgo during the first half of the third observing run, Phys. Rev. X **11**, 021053 (2021).

[3] R. Abbott (LIGO Scientific, Virgo, and KAGRA Collaborations), GWTC-3: Compact binary coalescences observed by LIGO and Virgo during the second part of the third observing run, Phys. Rev. X **13**, 041039 (2023).

[4] R. Abbott *et al.* (LIGO Scientific, and Virgo Collaborations), GW170817: Observation of gravitational waves from a binary neutron star inspiral, Phys. Rev. Lett. **119**, 161101 (2017).

[5] R. Abbott *et al.* (LIGO Scientific, and Virgo Collaborations), GW190412: Observation of a binary-black-hole coalescence with asymmetric masses, Phys. Rev. D **102**, 043015 (2020).

[6] R. Abbott *et al.* (LIGO Scientific, and Virgo Collaborations), GW190521: A binary black hole merger with a total mass of $150 M_{\odot}$, Phys. Rev. Lett. **125**, 101102 (2020).

[7] R. Abbott *et al.* (LIGO Scientific, and Virgo Collaborations), GW190814: Gravitational waves from the coalescence of a 23 solar mass black hole with a 2.6 solar mass compact object, Astrophys. J. Lett. **896**, L44 (2020).

[8] LIGO Scientific, Virgo, and KAGRA Collaborations, Observation of gravitational waves from the coalescence of a $2.5 - 4.5 M_{\odot}$ compact object and a neutron star, Astrophys. J. Lett. **970**, L34 (2024).

[9] The NANOGrav Collaboration, The NANOGrav 15 yr data set: Evidence for a gravitational-wave background, Astrophys. J. Lett. **951**, L8 (2023).

[10] P. Amaro-Seoane *et al.*, Astrophysics with the laser interferometer space antenna, Living Rev. Relativity **26**, 2 (2023).

[11] N. Aggarwal *et al.*, Challenges and opportunities of gravitational-wave searches at MHz to GHz frequencies, Living Rev. Relativity **24**, 4 (2021).

[12] A. Arvanitaki and A. A. Geraci, Detecting high-frequency gravitational waves with optically levitated sensors, Phys. Rev. Lett. **110**, 071105 (2013).

[13] N. Aggarwal, G. P. Winstone, M. Teo, M. Baryakhtar, S. L. Larson, V. Kalogera, and A. A. Geraci, Searching for new physics with a levitated-sensor-based gravitational-wave detector, Phys. Rev. Lett. **128**, 111101 (2022).

[14] G. Winstone, Z. Wang, S. Klomp, G. R. Felsted, A. Laeuger, C. Gupta, D. Grass, N. Aggarwal, J. Sprague, P. J. Pauzauskie, S. L. Larson, V. Kalogera, and A. A. Geraci (LSD Collaboration), Optical trapping of high-aspect-ratio NaYF hexagonal prisms for kHz-MHz gravitational wave detectors, Phys. Rev. Lett. **129**, 053604 (2022).

[15] S. R. Dolan, Instability of the massive Klein-Gordon field on the Kerr spacetime, Phys. Rev. D **76**, 084001 (2007).

[16] D. Baumann, H. S. Chia, J. Stout, and L. ter Haar, The spectra of gravitational atoms, J. Cosmol. Astropart. Phys. 12 (2019) 006.

[17] A. Arvanitaki and S. Dubovsky, Exploring the string axiverse with precision black hole physics, Phys. Rev. D **83**, 044026 (2011).

[18] R. D. Peccei and H. R. Quinn, CP conservation in the presence of pseudoparticles, Phys. Rev. Lett. **38**, 1440 (1977).

[19] S. Weinberg, A new light boson?, Phys. Rev. Lett. **40**, 223 (1978).

[20] F. Wilczek, Problem of strong p and t invariance in the presence of instantons, Phys. Rev. Lett. **40**, 279 (1978).

[21] B. Carr, K. Kohri, Y. Sendouda, and J. Yokoyama, Constraints on primordial black holes, Rep. Prog. Phys. **84**, 116902 (2021).

[22] E. D. Barr *et al.*, A pulsar in a binary with a compact object in the mass gap between neutron stars and black holes, Science **383**, 275 (2024).

[23] J. C. Siegel, I. Kiato, V. Kalogera, C. P. L. Berry, T. J. Maccarone, K. Breivik, J. J. Andrews, S. S. Bavera, A. Dotter, T. Fragos, K. Kovlakas, D. Misra, K. A. Rocha, P. M. Srivastava, M. Sun, Z. Xing, and E. Zapartas, Investigating the lower mass gap with low-mass X-ray binary population synthesis, Astrophys. J. **954**, 212 (2023).

[24] T. Sukhbold, T. Ertl, S. E. Woosley, J. M. Brown, and H. T. Janka, Core-collapse supernovae from 9 to 120 solar masses based on neutrino-powered explosions, Astrophys. J. **821**, 38 (2016).

[25] T. Ertl, S. E. Woosley, T. Sukhbold, and H. T. Janka, The explosion of helium stars evolved with mass loss, Astrophys. J. **890**, 51 (2020).

[26] K. Kruszyńska *et al.*, Lens parameters for Gaia18cbf—A long gravitational microlensing event in the Galactic plane, Astron. Astrophys. **662**, A59 (2022).

[27] D. Baumann, H. S. Chia, and R. A. Porto, Probing ultralight bosons with binary black holes, Phys. Rev. D **99**, 044001 (2019).

[28] W. Gautschi, Computational aspects of three-term recurrence relations, SIAM Rev. **9**, 24 (1967).

[29] S. J. Zhu, M. Baryakhtar, M. A. Papa, D. Tsuna, N. Kawanaka, and H.-B. Eggenstein, Characterizing the continuous gravitational-wave signal from boson clouds around Galactic isolated black holes, Phys. Rev. D **102**, 063020 (2020).

[30] M. Isi, L. Sun, R. Brito, and A. Melatos, Directed searches for gravitational waves from ultralight bosons, Phys. Rev. D **99**, 084042 (2019).

[31] C. Yuan, R. Brito, and V. Cardoso, Probing ultralight dark matter with future ground-based gravitational-wave detectors, Phys. Rev. D **104**, 044011 (2021).

[32] H. Yoshino and H. Kodama, Gravitational radiation from an axion cloud around a black hole: Superradiant phase, Prog. Theor. Exp. Phys. **2014**, 043E02 (2014).

[33] A. Irrgang, B. Wilcox, E. Tucker, and L. Schiefelbein, Milky Way mass models for orbit calculations, Astron. Astrophys. **549**, A137 (2013).

[34] W. M. Farr, N. Sravan, A. Cantrell, L. Kreidberg, C. D. Bailyn, I. Mandel, and V. Kalogera, The mass distribution of stellar-mass black holes, Astrophys. J. **741**, 103 (2011).

[35] M. C. Miller and J. M. Miller, The masses and spins of neutron stars and stellar-mass black holes, Phys. Rep. **548**, 1 (2015).

[36] Y. Shao and X.-D. Li, Population synthesis of black hole X-ray binaries, Astrophys. J. **898**, 143 (2020).

[37] K. C. Sahu *et al.* (RoboNet Collaboration), An isolated stellar-mass black hole detected through astrometric microlensing, Astrophys. J. **933**, 83 (2022).

[38] K. El-Badry *et al.*, A sun-like star orbiting a black hole, Mon. Not. R. Astron. Soc. **518**, 1057 (2023).

[39] C. L. Fryer, K. Belczynski, G. Wiktorowicz, M. Dominik, V. Kalogera, and D. E. Holz, Compact remnant mass function: Dependence on the explosion mechanism and metallicity, Astrophys. J. **749**, 91 (2012).

[40] C. S. Reynolds, Observational constraints on black hole spin, Annu. Rev. Astron. Astrophys. **59**, 117 (2021).

[41] M. Kilic, J. A. Munn, H. C. Harris, T. von Hippel, J. W. Liebert, K. A. Williams, E. Jeffery, and S. DeGennaro, The ages of the thin disk, thick disk, and the halo from nearby white dwarfs, Astrophys. J. **837**, 162 (2017).

[42] A. Helmi, Streams, substructures, and the early history of the Milky Way, Annu. Rev. Astron. Astrophys. **58**, 205 (2020).

[43] P. J. McMillan, Mass models of the Milky Way, Mon. Not. R. Astron. Soc. **414**, 2446 (2011).

[44] M. Jurić *et al.*, The Milky Way tomography with SDSS. I. Stellar number density distribution, Astrophys. J. **673**, 864 (2008).

[45] N. Bissantz and O. Gerhard, Spiral arms, bar shape and bulge microlensing in the Milky Way, Mon. Not. R. Astron. Soc. **330**, 591 (2002).

[46] R. Diehl, H. Halloin, K. Kretschmer, G. G. Lichti, V. Schönfelder, A. W. Strong, A. von Kienlin, W. Wang, P. Jean, J. Knödlseder, J.-P. Roques, G. Weidenspointner, S. Schanne, D. H. Hartmann, C. Winkler, and C. Wunderer, Radioactive ^{26}Al from massive stars in the Galaxy, Nature (London) **439**, 45 (2006).

[47] A. Olejak, K. Belczynski, T. Bulik, and M. Sobolewska, Synthetic catalog of black holes in the Milky Way, Astron. Astrophys. **638**, A94 (2020).

[48] E. Agol and M. Kamionkowski, X-rays from isolated black holes in the Milky Way, Mon. Not. R. Astron. Soc. **334**, 553 (2002).

[49] K. Riles, Searches for continuous-wave gravitational radiation, Living Rev. Relativity **26**, 3 (2023).

[50] N. Siemonsen and W. E. East, Gravitational wave signatures of ultralight vector bosons from black hole superradiance, Phys. Rev. D **101**, 024019 (2020).

[51] E. W. Leaver, An analytic representation for the quasinormal modes of Kerr black holes, Proc. R. Soc. A **402**, 285 (1985).

[52] E. Berti, V. Cardoso, and M. Casals, Eigenvalues and eigenfunctions of spin-weighted spheroidal harmonics in four and higher dimensions, Phys. Rev. D **73**, 024013 (2006).